

Nonlinear finite element model for 3D Galfenol systems

Suryarghya Chakrabarti and Marcelo J Dapino

Department of Mechanical and Aerospace Engineering, Ohio State University, Columbus, OH 43210, USA

E-mail: chakrabarti.3@osu.edu and dapino.1@osu.edu

Received 28 March 2011, in final form 27 July 2011

Published 30 September 2011

Online at stacks.iop.org/SMS/20/105034

Abstract

This work addresses the development of an advanced modeling tool which describes the full nonlinear coupling in three-dimensional (3D) Galfenol transducers to provide system level input–output relationships. Maxwell's equations for electromagnetics and Navier's equations for mechanical systems are formulated in weak form. The constitutive behavior of Galfenol is described through a nonlinear discrete energy-averaged model. The overall system is approximated hierarchically; first, piecewise linearization is used to describe quasi-static responses and magnetic bias calculations. A linear dynamic solution with piezomagnetic coefficients computed at a given magnetic bias describes the system dynamics for moderate inputs. Dynamic responses at large input fields and stresses are quantified through an implicit dynamic solution based on the trapezoidal rule. The model simultaneously incorporates the effects of eddy currents, flux leakage, structural dynamics and nonlinear material behavior. A case study on a Galfenol unimorph actuator validates the model in quasistatic and dynamic conditions.

(Some figures in this article are in colour only in the electronic version)

1. Introduction

Magnetostrictive iron–gallium alloys ($\text{Fe}_{100-x}\text{Ga}_x$, $x \approx 20\%$ Ga, known as Galfenol) possess structural-grade mechanical properties in addition to exhibiting moderate magnetostriction. These properties make Galfenol uniquely well suited for integration within three-dimensional (3D) active structures. Galfenol can be used in sensors or actuators capable of withstanding tension, compression and shock loads. To design Galfenol structures, a modeling framework is required for describing the full nonlinear coupling between the electrical, magnetic and mechanical domains. A Galfenol system consists of a Galfenol driver (likely with complex 3D geometry), passive magnetic materials for flux completion, passive structural materials for load transmission, permanent magnetic materials for magnetic biasing, and copper coils for generation of dynamic magnetic fields.

The development of coupled models for magnetostrictive transducers has received significant attention. Prior to the advent of Galfenol, this type of modeling was primarily focused on Terfenol-D ($\text{Tb}_{0.3}\text{Dy}_{0.7}\text{Fe}_{1.9}$). Dapino *et al* [1] coupled the Jiles–Atherton model with a wave equation

describing the structural dynamics of a Terfenol-D actuator. Huang *et al* [2] coupled a lumped parameter vibratory model with an extended version of the Jiles–Atherton equations which included a phenomenological description of eddy current losses [3]. Sarawate and Dapino [4] developed a unidirectionally coupled model in which eddy currents in the magnetostrictive sample are described by solving the 1D magnetic field diffusion equation.

Higher-dimensional models have also been proposed. Benbouzid [5] formulated a 2D bidirectionally coupled magnetostatic model with Terfenol-D constitutive behavior incorporated using surface splines. Kannan and Dasgupta [6] formulated a 2D magnetostatic model with bidirectionally coupled magnetomechanical relations, current-induced magnetic fields and electromagnetic body forces. Zhou *et al* [7] developed a dynamic finite element model of a unimorph actuator with one-way magnetomechanical coupling. The one-way coupled 3D model of Kim and Jung [8] quantifies the magnetostrictive force driving a coupled fluid-structural model for a sonar transducer.

All of these models take externally applied fields as input or compute the magnetic fields explicitly as a function

of applied currents. The following models attempt to describe the full coupling between the electromagnetic and mechanical boundary value problems. Aparicio and Sosa [9] presented a 3D, fully coupled finite element model including dynamic effects in the context of a simple single-element magnetostrictive transducer. Slaughter [10] implemented a finite element model based on linear piezomagnetic relations which couples the structural mechanics and AC/DC modules in the commercial package COMSOL. Mudivarthi *et al* [11] utilized a fully coupled, magnetostatic formulation to describe stress-induced flux density changes in Galfenol with no current-induced fields. An updated version of the model includes current-induced magnetic fields but not eddy current losses; thus this model is magnetostatic [12]. In order to describe transducer level input–output relationships for dynamic inputs, Evans and Dapino [13] presented a fully coupled dynamic model for 3D magnetostrictive transducers. The model simultaneously quantifies the effects of eddy currents, structural dynamics, and flux leakage on transducer performance. Due to the restriction of COMSOL Multiphysics being unable to handle vectorized functions, linear constitutive behavior is assumed.

This paper extends the framework by Evans and Dapino [13] into nonlinear Galfenol regimes through the use of an efficient discrete energy-averaged model (DEAM) [14]. The weak form equations are entered into COMSOL (version 3.5a), which is used to assemble the inertia, damping, and stiffness matrices, the latter being recalculated at each time step. A custom Matlab script (version R2009a) is used to approximate solutions to the matrix system. Section 2 gives a brief description of the weak form model equations, followed by the DEAM and its analytical differentiation which yields the material Jacobian matrix (matrix of material coefficients) in section 3. For quasi-static operation, an efficient piecewise linear solution strategy is proposed in section 4 in which Galfenol constitutive behavior is implemented by solving the linear piezomagnetic equations in piecewise increments. At the end of each step the Galfenol material coefficients are updated using the computed material Jacobian. This piecewise linear solution strategy is useful for obtaining accurate magnetic bias points. A linear dynamic simulation with Galfenol coefficients computed at a given bias point describes the system dynamics for moderate excitations. Finally, an implicit time-integration algorithm is discussed in section 6 to obtain the dynamic system response for large inputs. Comparison of these solutions with experiments conducted on a Galfenol unimorph actuator are presented in sections 5 and 7.

2. Weak form equations

The aim of the finite element model is to obtain the electromagnetic quantities, magnetic flux density (\mathbf{B}), magnetic field (\mathbf{H}), electric flux density (\mathbf{D}), and electric field (\mathbf{E}), and the mechanical quantities, stress (\mathbf{T}) and strain (\mathbf{S}), in the system. The electrical and magnetic variables can be related using Maxwell's equations:

$$\nabla \times \mathbf{E} = -\frac{\partial \mathbf{B}}{\partial t}, \quad (1)$$

$$\nabla \cdot \mathbf{D} = \rho_q, \quad (2)$$

$$\nabla \times \mathbf{H} = \mathbf{J} + \frac{\partial \mathbf{D}}{\partial t}, \quad (3)$$

$$\nabla \cdot \mathbf{B} = 0, \quad (4)$$

where ρ_q and \mathbf{J} are the free charge and free current density, respectively. The mechanical variables can be described using Navier's equation:

$$\rho \frac{\partial^2 \mathbf{u}}{\partial t^2} + c \frac{\partial \mathbf{u}}{\partial t} = \nabla \cdot \mathbf{T} + \mathbf{f}_B, \quad (5)$$

where \mathbf{u} is the displacement vector, ρ is the mass density, c is the structural damping coefficient, and \mathbf{f}_B is the vector of body forces. Almost all formulations for electromechanical systems use a standard displacement-based formulation for the mechanical subsystem, meaning the solution variables are the mechanical displacements at the nodes of the model. Strain is obtained using the globally defined gradient operation on the displacement field, while stress is obtained using constitutive laws. For the electromagnetic subsystem, different approaches are followed. Magnetostatic problems are often modeled using a scalar magnetic potential [6] in which the magnetic field is split up into a magnetization-induced component computed as the gradient of the scalar magnetic potential and an externally imposed component entered as nodal force terms. The advantage of this procedure is that constitutive laws do not have to be inverted since most constitutive models take the magnetic field as an input. The disadvantage of this formulation is that the current-induced fields need to be specified manually but they generally are unknown before solving the system. For the same reason, the formulation is restricted to quasi-static operating conditions in which eddy currents are absent. Formulations based on vector magnetic potentials [9, 13] are more appropriate for dynamic modeling of magnetostrictive transducers since they allow direct inclusion of source current densities along with eddy current-induced flux density changes. The vector magnetic potential \mathbf{A} is defined as

$$\mathbf{B} = \nabla \times \mathbf{A}. \quad (6)$$

With this definition, Gauss' law (4) is identically satisfied. The second term in (3) describes displacement currents and can be neglected within the frequency bandwidth of magnetostrictive transducers (<30 kHz). Lorentz forces are neglected since the only component containing a significantly large current density in a magnetostrictive transducer is the drive coil which is structurally inactive. Finally, voltage gradients are neglected; the only source of electrical input is considered to be a source current density (\mathbf{J}_s) applied to the coil. Under these assumptions the only one of Maxwell's equations to be solved is (3), which is reduced to

$$\nabla \times \mathbf{H} = \mathbf{J}_s - \sigma \frac{\partial \mathbf{A}}{\partial t}, \quad (7)$$

with σ the electric conductivity of the material. The second term on the right-hand side quantifies eddy currents in electrically conducting materials. The weak form equations

can be derived using the method of weighted residuals as done by Evans and Dapino [13],

$$\int_{V_B} \mathbf{H} \cdot \delta \mathbf{B} dV + \int_{V_B} \sigma \frac{\partial \mathbf{A}}{\partial t} \cdot \delta \mathbf{A} dV = \int_{\partial V_B} (\mathbf{H} \times \mathbf{n}) \cdot \delta \mathbf{A} d\partial V + \int_{V_B} \mathbf{J}_s \cdot \delta \mathbf{A} dV, \quad (8)$$

$$\int_{V_u} \mathbf{T} \cdot \delta \mathbf{S} dV + \int_{V_u} \left(\rho \frac{\partial^2 \mathbf{u}}{\partial t^2} + c \frac{\partial \mathbf{u}}{\partial t} \right) \cdot \delta \mathbf{u} dV = \int_{\partial V_u} \mathbf{t} \cdot \delta \mathbf{u} d\partial V + \int_{V_u} \mathbf{f}_B \cdot \delta \mathbf{u} dV. \quad (9)$$

The solution variables are the mechanical displacement field (\mathbf{u}) and the vector magnetic potential (\mathbf{A}). Equations (8) and (9) are decoupled in all domains except in Galfenol where the mechanical and magnetic states are coupled in a nonlinear manner. The first term in (8) and (9) suggests that the constitutive law should take (\mathbf{B} , \mathbf{S}) as inputs and calculate (\mathbf{H} , \mathbf{T}) as outputs. Almost all constitutive models work the other way around, thus requiring inversion for incorporation in (8) and (9). Since the models are nonlinear in nature, analytical inversion is in most cases impossible. Sections 4 and 6 discuss the techniques used to incorporate the nonlinear Galfenol constitutive law in the model.

3. Discrete energy-averaged model (DEAM)

Incorporation of nonlinear constitutive behavior poses a significant challenge in the formulation of coupled finite element models for magnetostrictive systems. Magnetostrictive material behavior is often described by polynomial fitting of data. For example, Benbouzid *et al* [15] used surface splines to fit experimental data while Kannan and Dasgupta [6] used constitutive relations in an incremental form with coefficients obtained from bicubic spline fits to measurements. Kim *et al* [8] used sixth-order polynomials to fit the strain field behavior with a different set of coefficients for each preload condition. The use of spline functions has the advantages of easy differentiability and implementation for 1D cases. However, this procedure is complex when complete 3D material behavior is required. This would require 3D measurements to be performed and bulky splines with nine components (three for field and six for stress) to be fitted to those measurements. Graham *et al* [12] implemented Galfenol constitutive behavior through look-up tables generated *a priori* using the Armstrong model for a large number of induction and stress values. Although the Armstrong model is three-dimensional, look-up tables were generated for 1D induction and stress inputs. As is the case with splines, extension to a full 3D version is complex because it requires generation of large tables with nine inputs and nine outputs. For these reasons, using an efficient constitutive law coded up as functions is beneficial for 3D boundary value problems.

The energy-averaged class of models describes macroscopic material response based on an energy-weighted summation of contributions from domains aligned along different orientations. With homogeneously distributed fixed orientations (as in Armstrong's model [16]), obtaining high accuracy requires a large number of possible orientations

to be considered which results in significant computational effort. Atulasimha *et al* [17] improved the efficiency of these models by tracking the volume fractions of domains aligned along 98 fixed orientations. To preserve accuracy along with computational efficiency, Evans and Dapino [14] restricted the number of possible orientations to six by considering only the directions which minimize an energy functional locally defined around each easy axis. The total free energy of a domain close to the k th easy axis \mathbf{c}^k is formulated as the sum of local anisotropy energy, magnetomechanical coupling energy, and Zeeman energy as

$$G^k = \frac{1}{2} K^k |\mathbf{m}^k - \mathbf{c}^k|^2 - \mathbf{S}_m^k \cdot \mathbf{T} - \mu_0 M_s \mathbf{m}^k \cdot \mathbf{H}, \quad (10)$$

which must be minimized with respect to the orientation vector \mathbf{m}^k in the vicinity of \mathbf{c}^k . The magnetostriction tensor \mathbf{S}_m^k of a cubic material is

$$\mathbf{S}_m^k = \begin{Bmatrix} (3/2)\lambda_{100}(m_1^k)^2 \\ (3/2)\lambda_{100}(m_2^k)^2 \\ (3/2)\lambda_{100}(m_3^k)^2 \\ 3\lambda_{111}m_1^k m_2^k \\ 3\lambda_{111}m_2^k m_3^k \\ 3\lambda_{111}m_3^k m_1^k \end{Bmatrix}. \quad (11)$$

The minimization problem is constrained ($\|\mathbf{m}^k\| = 1$) and is formulated as an inhomogeneous eigenvalue problem through the use of Lagrange multipliers. The total energy is written as

$$G^k = \frac{1}{2} \mathbf{m}^k \cdot \mathbf{K}^k \mathbf{m}^k - \mathbf{m}^k \cdot \mathbf{B}^k, \quad (12)$$

where the magnetic stiffness matrix \mathbf{K}^k and force vector \mathbf{B}^k are

$$\mathbf{K}^k = \begin{bmatrix} K^k - 3\lambda_{100}T_1 & -3\lambda_{111}T_4 & -3\lambda_{111}T_6 \\ -3\lambda_{111}T_4 & K^k - 3\lambda_{100}T_2 & -3\lambda_{111}T_5 \\ -3\lambda_{111}T_6 & -3\lambda_{111}T_5 & K^k - 3\lambda_{100}T_3 \end{bmatrix}, \quad (13)$$

$$\mathbf{B}^k = [c_1^k K^k + \mu_0 M_s H_1 \quad c_2^k K^k + \mu_0 M_s H_2 \quad c_3^k K^k + \mu_0 M_s H_3]^T. \quad (14)$$

The Lagrange function is constructed as the sum of the energy functional and the unity norm constraint on the orientation vectors linearized about the easy-axis orientations ($\mathbf{m}^k \cdot \mathbf{m}^k = 1 \approx \mathbf{c}^k \cdot \mathbf{m}^k = 1$),

$$L = \frac{1}{2} \mathbf{m}^k \cdot \mathbf{K}^k \mathbf{m}^k - \mathbf{m}^k \cdot \mathbf{B}^k + \lambda^k (\mathbf{c}^k \cdot \mathbf{m}^k - 1), \quad (15)$$

where λ^k is the Lagrange multiplier corresponding to the k th easy axis. Differentiating the Lagrange function with respect to \mathbf{m}^k and equating to zero one gets

$$\mathbf{m}^k = \mathbf{K}^{k-1} [\mathbf{B}^k - \lambda^k \mathbf{c}^k]. \quad (16)$$

Substitution of \mathbf{m}^k from (16) into the above constraint yields the following expression for the Lagrange multiplier:

$$\lambda^k = -\frac{1 - \mathbf{c}^k \cdot (\mathbf{K}^k)^{-1} \mathbf{B}^k}{\mathbf{c}^k \cdot (\mathbf{K}^k)^{-1} \mathbf{c}^k}, \quad (17)$$

which upon substitution into (16) gives an analytical expression for the orientation which minimizes the energy around the k th easy axis,

$$\mathbf{m}^k = (\mathbf{K}^k)^{-1} \left[\mathbf{B}^k + \frac{1 - \mathbf{c}^k \cdot (\mathbf{K}^k)^{-1} \mathbf{B}^k}{\mathbf{c}^k \cdot (\mathbf{K}^k)^{-1} \mathbf{c}^k} \mathbf{c}^k \right]. \quad (18)$$

At very high fields well in the saturation regime, the norm of \mathbf{m}^k can become much greater than unity, thus yielding unphysical magnetization and strain calculations. This issue can be addressed by strictly enforcing the unity norm constraint rather than using the approximation $\mathbf{m}^k \cdot \mathbf{m}^k = 1 \approx \mathbf{c}^k \cdot \mathbf{m}^k = 1$. However, that leads to a sixth order equation for the Lagrange multiplier for which no analytical solution is possible. To circumvent the issue of unphysical magnetization and strain due to the linearized norm constraint, \mathbf{m}^k is divided by its norm in subsequent calculations and is denoted by the symbol $(\hat{\mathbf{m}}^k)$.

The anhysteretic volume fractions are calculated explicitly using Boltzmann-type averaging:

$$\xi_{\text{an}}^k = \frac{\exp(-G^k/\Omega)}{\sum_{j=1}^r \exp(-G^j/\Omega)}, \quad (19)$$

where Ω is an averaging factor. Macroscopic anhysteretic material behavior is obtained by summing the individual contributions of each domain weighted by its corresponding volume fraction. The bulk magnetization \mathbf{M} and strain \mathbf{S} are obtained by averaging the properties along the six minima weighted by their respective volume fractions,

$$\mathbf{M} = M_s \sum_{k=1}^r \xi_{\text{an}}^k \hat{\mathbf{m}}^k, \quad (20)$$

$$\mathbf{S} = \mathbf{sT} + \sum_{k=1}^r \xi_{\text{an}}^k \mathbf{S}_{\text{m}}^k. \quad (21)$$

The DEAM is extremely efficient since it includes energy-weighted summation of only six terms and analytical expressions to calculate the minima. Moreover, it can be analytically differentiated to obtain the matrix of material coefficients. This property is useful for formulating the piecewise linear solution procedure described in section 4, as well as in the numerical inversion process for the nonlinear dynamic solution discussed in section 6.

3.1. Evaluating the material Jacobian

Evaluation of the material Jacobian requires computation of the derivatives $\partial \mathbf{B}/\partial \mathbf{H}$, $\partial \mathbf{B}/\partial \mathbf{T}$, $\partial \mathbf{S}/\partial \mathbf{H}$, and $\partial \mathbf{S}/\partial \mathbf{T}$. The tensors \mathbf{S} and \mathbf{T} are written in contracted notation. The derivatives are obtained with respect to H_i ($i = 1-3$) and T_i ($i = 1-6$). Magnetic induction is algebraically related to magnetic field and magnetization,

$$\mathbf{B} = \mu_0 (\mathbf{H} + \mathbf{M}). \quad (22)$$

The derivatives of \mathbf{B} with respect to T_i and H_i are

$$\frac{\partial \mathbf{B}}{\partial T_i} = \mu_0 \left(\frac{\partial \mathbf{M}}{\partial T_i} \right), \quad (23)$$

$$\frac{\partial \mathbf{B}}{\partial H_i} = \mu_0 \left(\frac{\partial \mathbf{H}}{\partial H_i} + \frac{\partial \mathbf{M}}{\partial H_i} \right). \quad (24)$$

The derivatives of \mathbf{M} and \mathbf{S} with respect to H_i and T_i can be obtained by differentiating (20) and (21):

$$\frac{\partial \mathbf{M}}{\partial H_i} = \sum_{k=1}^r M_s \left(\frac{\partial \hat{\mathbf{m}}^k}{\partial H_i} \xi_{\text{an}}^k + \hat{\mathbf{m}}^k \frac{\partial \xi_{\text{an}}^k}{\partial H_i} \right), \quad (25)$$

$$\frac{\partial \mathbf{M}}{\partial T_i} = \sum_{k=1}^r M_s \left(\frac{\partial \hat{\mathbf{m}}^k}{\partial T_i} \xi_{\text{an}}^k + \hat{\mathbf{m}}^k \frac{\partial \xi_{\text{an}}^k}{\partial T_i} \right), \quad (26)$$

$$\frac{\partial \mathbf{S}}{\partial H_i} = \sum_{k=1}^r \left(\frac{\partial \mathbf{S}_{\text{m}}^k}{\partial H_i} \xi_{\text{an}}^k + \mathbf{S}_{\text{m}}^k \frac{\partial \xi_{\text{an}}^k}{\partial H_i} \right), \quad (27)$$

$$\frac{\partial \mathbf{S}}{\partial T_i} = \mathbf{s} \frac{\partial \mathbf{T}}{\partial T_i} + \sum_{k=1}^r \left(\frac{\partial \mathbf{S}_{\text{m}}^k}{\partial T_i} \xi_{\text{an}}^k + \mathbf{S}_{\text{m}}^k \frac{\partial \xi_{\text{an}}^k}{\partial T_i} \right). \quad (28)$$

Thus, the partial derivatives of $\hat{\mathbf{m}}^k$, \mathbf{S}_{m}^k and ξ_{an}^k with respect to H_i and T_i must be obtained. The derivatives of \mathbf{S}_{m}^k can be written as

$$\begin{aligned} \frac{\partial \mathbf{S}_{\text{m}}^k}{\partial H_i} &= \begin{Bmatrix} 3\lambda_{100} \hat{m}_1^k \frac{\partial \hat{m}_1^k}{\partial H_i} \\ 3\lambda_{100} \hat{m}_2^k \frac{\partial \hat{m}_2^k}{\partial H_i} \\ 3\lambda_{100} \hat{m}_3^k \frac{\partial \hat{m}_3^k}{\partial H_i} \\ 3\lambda_{111} \left(\hat{m}_1^k \frac{\partial \hat{m}_2^k}{\partial H_i} + \hat{m}_2^k \frac{\partial \hat{m}_1^k}{\partial H_i} \right) \\ 3\lambda_{111} \left(\hat{m}_2^k \frac{\partial \hat{m}_3^k}{\partial H_i} + \hat{m}_3^k \frac{\partial \hat{m}_2^k}{\partial H_i} \right) \\ 3\lambda_{111} \left(\hat{m}_3^k \frac{\partial \hat{m}_1^k}{\partial H_i} + \hat{m}_1^k \frac{\partial \hat{m}_3^k}{\partial H_i} \right) \end{Bmatrix}, \\ \frac{\partial \mathbf{S}_{\text{m}}^k}{\partial T_i} &= \begin{Bmatrix} 3\lambda_{100} \hat{m}_1^k \frac{\partial \hat{m}_1^k}{\partial T_i} \\ 3\lambda_{100} \hat{m}_2^k \frac{\partial \hat{m}_2^k}{\partial T_i} \\ 3\lambda_{100} \hat{m}_3^k \frac{\partial \hat{m}_3^k}{\partial T_i} \\ 3\lambda_{111} \left(\hat{m}_1^k \frac{\partial \hat{m}_2^k}{\partial T_i} + \hat{m}_2^k \frac{\partial \hat{m}_1^k}{\partial T_i} \right) \\ 3\lambda_{111} \left(\hat{m}_2^k \frac{\partial \hat{m}_3^k}{\partial T_i} + \hat{m}_3^k \frac{\partial \hat{m}_2^k}{\partial T_i} \right) \\ 3\lambda_{111} \left(\hat{m}_3^k \frac{\partial \hat{m}_1^k}{\partial T_i} + \hat{m}_1^k \frac{\partial \hat{m}_3^k}{\partial T_i} \right) \end{Bmatrix}. \end{aligned} \quad (29)$$

The derivative of ξ_{an}^k with respect to H_i and T_i can be found by differentiating (19):

$$\frac{\partial \xi_{\text{an}}^k}{\partial H_i} = \frac{\xi_{\text{an}}^k}{\Omega} \left[\sum_{j=1}^r \xi_{\text{an}}^j \left(\frac{\partial G^j}{\partial H_i} \right) - \left(\frac{\partial G^k}{\partial H_i} \right) \right], \quad (30)$$

$$\frac{\partial \xi_{\text{an}}^k}{\partial T_i} = \frac{\xi_{\text{an}}^k}{\Omega} \left[\sum_{j=1}^r \xi_{\text{an}}^j \left(\frac{\partial G^j}{\partial T_i} \right) - \left(\frac{\partial G^k}{\partial T_i} \right) \right]. \quad (31)$$

The derivatives of G^k with respect to H_i and T_i are

$$\frac{\partial G^k}{\partial H_i} = \hat{\mathbf{m}}^k \cdot \mathbf{K}^k \left(\frac{\partial \hat{\mathbf{m}}^k}{\partial H_i} \right) - \frac{\partial \hat{\mathbf{m}}^k}{\partial H_i} \cdot \mathbf{B}^k - \hat{\mathbf{m}}^k \cdot \left(\frac{\partial \mathbf{B}^k}{\partial H_i} \right), \quad (32)$$

$$\frac{\partial G^k}{\partial T_i} = \hat{\mathbf{m}}^k \cdot \mathbf{K}^k \left(\frac{\partial \hat{\mathbf{m}}^k}{\partial T_i} \right) + \frac{1}{2} \hat{\mathbf{m}}^k \cdot \left(\frac{\partial \mathbf{K}^k}{\partial T_i} \right) \hat{\mathbf{m}}^k - \frac{\partial \hat{\mathbf{m}}^k}{\partial T_i} \cdot \mathbf{B}^k. \quad (33)$$

The derivatives of the normalized k th equilibrium orientation with respect to H_i and T_i are

$$\frac{\partial \hat{\mathbf{m}}^k}{\partial H_i} = \frac{1}{\|\mathbf{m}^k\|} (\mathbf{K}^k)^{-1} \left[\frac{\partial \mathbf{B}^k}{\partial H_i} - \left(\frac{\mathbf{c}^k \cdot (\mathbf{K}^k)^{-1} \frac{\partial \mathbf{B}^k}{\partial H_i}}{\mathbf{c}^k \cdot (\mathbf{K}^k)^{-1} \mathbf{c}^k} \right) \mathbf{c}^k \right] - \frac{\mathbf{m}^k}{\|\mathbf{m}^k\|^3} \left(\mathbf{m}^k \cdot (\mathbf{K}^k)^{-1} \left[\frac{\partial \mathbf{B}^k}{\partial H_i} - \left(\frac{\mathbf{c}^k \cdot (\mathbf{K}^k)^{-1} \frac{\partial \mathbf{B}^k}{\partial H_i}}{\mathbf{c}^k \cdot (\mathbf{K}^k)^{-1} \mathbf{c}^k} \right) \mathbf{c}^k \right] \right), \quad (34)$$

$$\frac{\partial \hat{\mathbf{m}}^k}{\partial T_i} = \frac{1}{\|\mathbf{m}^k\|} (\mathbf{K}^k)^{-1} \left[- \left(\frac{\partial \mathbf{K}^k}{\partial T_i} \right) \mathbf{m}^k + \frac{\mathbf{c}^k \cdot ((\mathbf{K}^k)^{-1} \frac{\partial \mathbf{K}^k}{\partial T_i} \mathbf{m}^k)}{\mathbf{c}^k \cdot (\mathbf{K}^k)^{-1} \mathbf{c}^k} \mathbf{c}^k \right] - \frac{\mathbf{m}^k}{\|\mathbf{m}^k\|^3} \left(\mathbf{m}^k \cdot (\mathbf{K}^k)^{-1} \times \left[- \left(\frac{\partial \mathbf{K}^k}{\partial T_i} \right) \mathbf{m}^k + \frac{\mathbf{c}^k \cdot ((\mathbf{K}^k)^{-1} \frac{\partial \mathbf{K}^k}{\partial T_i} \mathbf{m}^k)}{\mathbf{c}^k \cdot (\mathbf{K}^k)^{-1} \mathbf{c}^k} \mathbf{c}^k \right] \right), \quad (35)$$

where

$$\frac{\partial \mathbf{B}^k}{\partial H_1} = \begin{Bmatrix} \mu_0 M_s \\ 0 \\ 0 \end{Bmatrix}, \quad \frac{\partial \mathbf{B}^k}{\partial H_2} = \begin{Bmatrix} 0 \\ \mu_0 M_s \\ 0 \end{Bmatrix}, \quad \frac{\partial \mathbf{B}^k}{\partial H_3} = \begin{Bmatrix} 0 \\ 0 \\ \mu_0 M_s \end{Bmatrix}, \quad (36)$$

and

$$\begin{aligned} \frac{\partial \mathbf{K}^k}{\partial T_1} &= \begin{bmatrix} -3\lambda_{100} & 0 & 0 \\ 0 & 0 & 0 \\ 0 & 0 & 0 \end{bmatrix}, \\ \frac{\partial \mathbf{K}^k}{\partial T_4} &= \begin{bmatrix} 0 & -3\lambda_{111} & 0 \\ -3\lambda_{111} & 0 & 0 \\ 0 & 0 & 0 \end{bmatrix}, \\ \frac{\partial \mathbf{K}^k}{\partial T_2} &= \begin{bmatrix} 0 & 0 & 0 \\ 0 & -3\lambda_{100} & 0 \\ 0 & 0 & 0 \end{bmatrix}, \\ \frac{\partial \mathbf{K}^k}{\partial T_5} &= \begin{bmatrix} 0 & 0 & 0 \\ 0 & 0 & -3\lambda_{111} \\ 0 & -3\lambda_{111} & 0 \end{bmatrix}, \\ \frac{\partial \mathbf{K}^k}{\partial T_3} &= \begin{bmatrix} 0 & 0 & 0 \\ 0 & 0 & 0 \\ 0 & 0 & -3\lambda_{100} \end{bmatrix}, \\ \frac{\partial \mathbf{K}^k}{\partial T_6} &= \begin{bmatrix} 0 & 0 & -3\lambda_{111} \\ 0 & 0 & 0 \\ -3\lambda_{111} & 0 & 0 \end{bmatrix}. \end{aligned} \quad (37)$$

Thus the derivatives of $\hat{\mathbf{m}}^k$, \mathbf{S}_m^k and ξ_{an}^k with respect to H_i and T_i are known. Plugging these back into (25)–(28) the derivatives of \mathbf{M} and \mathbf{S} with respect to H_i and T_i are obtained. Further, the derivatives of \mathbf{B} with respect to H_i and T_i are computed by plugging (25) and (26) into (23) and (24) giving all the derivatives required to compute the Jacobian.

4. Piecewise linear solution procedure

Under quasi-static conditions, the weak form equations (8) and (9) can be written in incremental form as

$$\int_{V_B} \Delta \mathbf{H} \cdot \delta \Delta \mathbf{B} dV = \int_{\partial V_B} (\Delta \mathbf{H} \times \mathbf{n}) \cdot \delta \Delta \mathbf{A} d\partial V + \int_{V_B} \Delta \mathbf{J}_s \cdot \delta \Delta \mathbf{A} dV, \quad (38)$$

$$\int_{V_u} \Delta \mathbf{T} \cdot \delta \Delta \mathbf{S} dV = \int_{\partial V_u} \Delta \mathbf{t} \cdot \delta \Delta \mathbf{u} d\partial V + \int_{V_u} \Delta \mathbf{f}_B \cdot \delta \Delta \mathbf{u} dV, \quad (39)$$

where $\Delta \mathbf{H}$ and $\Delta \mathbf{T}$ must be computed as a function of $\Delta \mathbf{B}$ and $\Delta \mathbf{S}$. For some field \mathbf{H}_0 and stress \mathbf{T}_0 , the DEAM computes \mathbf{B} and \mathbf{S} along with the material Jacobian \mathcal{J} given by

$$\mathcal{J} = \begin{bmatrix} \boldsymbol{\mu} = \frac{\partial \mathbf{B}}{\partial \mathbf{H}}(\mathbf{H}_0, \mathbf{T}_0) & \mathbf{d} = \frac{\partial \mathbf{B}}{\partial \mathbf{T}}(\mathbf{H}_0, \mathbf{T}_0) \\ \mathbf{d}^T = \frac{\partial \mathbf{S}}{\partial \mathbf{H}}(\mathbf{H}_0, \mathbf{T}_0) & \mathbf{s} = \frac{\partial \mathbf{S}}{\partial \mathbf{T}}(\mathbf{H}_0, \mathbf{T}_0) \end{bmatrix}. \quad (40)$$

For small deviations about \mathbf{H}_0 and \mathbf{T}_0 , the constitutive law can be formulated in incremental form through inversion of the material Jacobian matrix:

$$\begin{bmatrix} \Delta \mathbf{H} \\ \Delta \mathbf{T} \end{bmatrix} = \begin{bmatrix} \boldsymbol{\mu}^i & -\mathbf{a} \\ -\mathbf{a}^T & \mathbf{c} \end{bmatrix} \begin{bmatrix} \Delta \mathbf{B} \\ \Delta \mathbf{S} \end{bmatrix} = \mathcal{J}^{-1} \begin{bmatrix} \Delta \mathbf{B} \\ \Delta \mathbf{S} \end{bmatrix}. \quad (41)$$

Since the computed coefficients are dependent on stress and field, which have a spatial variation, the coefficients are also spatially variant. To preserve this inhomogeneity, the coefficients are declared as interpolated data functions of spatial coordinates. Each coefficient is a separate function and, when called, COMSOL searches in the data file for their values corresponding to that location or interpolates between nearby points if that location is not present in the file. Thirty three material coefficients are used:

$$\begin{aligned} \boldsymbol{\mu}^{-1} &= \begin{bmatrix} \mu_{11}^i & \mu_{12}^i & \mu_{13}^i \\ \mu_{12}^i & \mu_{22}^i & \mu_{23}^i \\ \mu_{13}^i & \mu_{23}^i & \mu_{33}^i \end{bmatrix}, \\ \mathbf{a} &= \begin{bmatrix} a_{11} & a_{12} & a_{13} & a_{14} & a_{15} & a_{16} \\ a_{21} & a_{22} & a_{23} & a_{24} & a_{25} & a_{26} \\ a_{31} & a_{32} & a_{33} & a_{34} & a_{35} & a_{36} \end{bmatrix}, \\ \mathbf{c} &= \begin{bmatrix} c_{11} & c_{12} & c_{13} & 0 & 0 & 0 \\ c_{12} & c_{22} & c_{23} & 0 & 0 & 0 \\ c_{13} & c_{23} & c_{33} & 0 & 0 & 0 \\ 0 & 0 & 0 & c_{44} & 0 & 0 \\ 0 & 0 & 0 & 0 & c_{55} & 0 \\ 0 & 0 & 0 & 0 & 0 & c_{66} \end{bmatrix}. \end{aligned} \quad (42)$$

Ideally, the coefficients must be evaluated at all the integration points present in the Galfenol subdomain during the assembly process. In a 3D model several thousand integration points are present. Evaluation, inversion and storage of the Jacobian at every integration point is both computationally and memory intensive. Assuming that the spatial variation in field and stress is not steep, the coefficients are calculated only at selected locations and approximated at the remaining points through interpolation.

Figure 1 shows a flowchart of the piecewise linear solution procedure. A custom Matlab script implements this algorithm. The computation is initialized with zero initial conditions and the piezomagnetic coefficients are updated by computing the material Jacobian at zero field and stress. A COMSOL script is

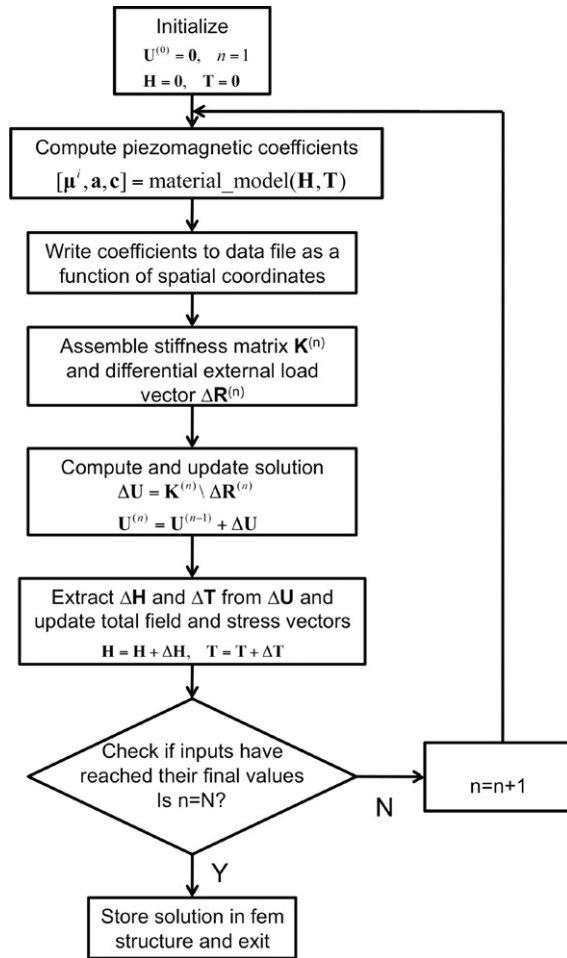


Figure 1. Flowchart of the piecewise linear solution process.

invoked to assemble the external load vector and the system matrix; subsequently, the incremental solution vector ($\Delta \mathbf{U}$) is computed. The next step is to obtain the stress and field increments from $\Delta \mathbf{U}$. Increments in induction ($\Delta \mathbf{B}$) and strain ($\Delta \mathbf{S}$) are found using the kinematic relationships with the vector magnetic potential and mechanical displacements. Next, $\Delta \mathbf{T}$ and $\Delta \mathbf{H}$ are obtained from $\Delta \mathbf{B}$ and $\Delta \mathbf{S}$ using the inverted constitutive law (41). The total field and stress vectors are updated with the corresponding increments. This process is repeated until the end of the input arrays is reached.

The computation is fast as it does not involve iteration loops or convergence checks. Consequently, the solution has a tendency to drift since within every interval a nonlinear response is approximated by linear behavior. The larger the size of each interval the larger the drift. Thus, depending on the desired accuracy, a sufficiently small step size must be utilized.

The piecewise linear model is useful for two purposes. First, to obtain a measure of quasi-static system performance and secondly to generate accurate bias points which preserve the spatial inhomogeneity in the distribution of field and stress in Galfenol and, hence, in the material coefficients. A measure of dynamic response for moderate inputs about the bias point can be obtained using these coefficients.

5. Piecewise linear model results

The finite element framework described in the previous sections is validated using the Galfenol unimorph actuator shown in figure 2(a). The actuator consists of a composite beam having a Galfenol layer bonded to a brass substrate, a stainless steel clamp, a drive coil, and a steel yoke. The system is excited by applying a voltage input to the coil; the vertical tip deflection of the beam is measured with a laser displacement sensor. Figure 2(b) shows the mesh geometry used for finite element calculations. The lower surface of the stainless steel clamp is mechanically fixed ($\mathbf{u} = 0$) to remove rigid body modes. The actuator is surrounded by a sufficiently large air volume such that the magnetic potential is negligible at its outer boundaries, $\mathbf{A} = 0$.

5.1. Piecewise linear quasi-static solution

Quasi-static measurements are collected by cycling the voltage at 0.1 Hz. In the model, input is applied in the form of small increments to the coil source current density and solution is obtained using the piecewise linear approach outlined in figure 1. Beam tip deflection is obtained by integrating the vertical displacement component over the free end of the Galfenol layer. The simulation accurately describes the nonlinearity in the beam deflection response (see figure 3). The voltage–current curve is a straight line whose slope is the dc resistance of the coil.

5.2. Linear dynamic simulation about bias point

Harmonic response of the beam is obtained by applying a bias voltage of 7 V and sinusoidal voltage inputs at different frequencies. The amplitude of the sinusoidal voltage signal is increased with increasing frequency to keep the current levels comparable so as to obtain a good measurable displacement response at the beam tip. Figures 4–8 show the time-domain current and displacement response of the system to sinusoidal voltage inputs ranging from 10 to 500 Hz. The model quantifies the transient dynamic behavior of the beam for all the frequencies using a single set of parameters. At the lower frequencies the model slightly overpredicts the response because of its linear nature. As the frequency increases, the inertia and damping forces dominate the force arising from the nonlinear internal stiffness, thus yielding a smoother response. This leads to better correlation between the amplitudes of the modeled and experimental curves. However, because the model does not include Galfenol hysteresis, there is a phase difference between the experimental and modeled curves which is negligible up to 100 Hz but becomes more noticeable at the higher frequencies. At 200 Hz the measured displacement response is distorted, possibly because some nonlinearities in the material are excited at that frequency due to a particular distribution of stress and field. Since the dynamic model is linear in nature, this effect is not described. The measured current response is undistorted and is accurately described. At 500 Hz the transient tip deflection response exhibits beating behavior, as the excitation frequency is close to the first natural frequency of the actuator (513 Hz). When

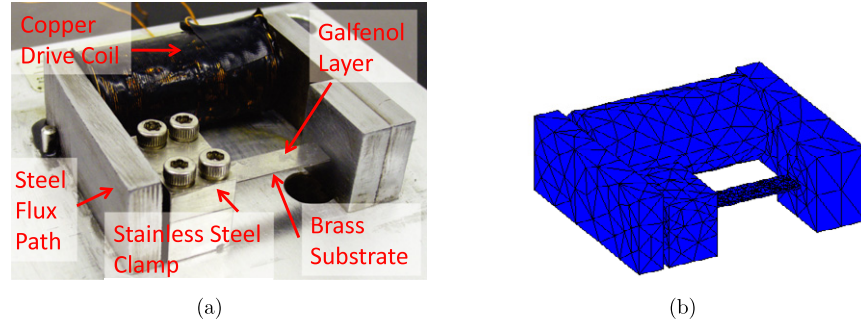


Figure 2. Galfenol unimorph actuator used for model validation: (a) geometry and (b) mesh.

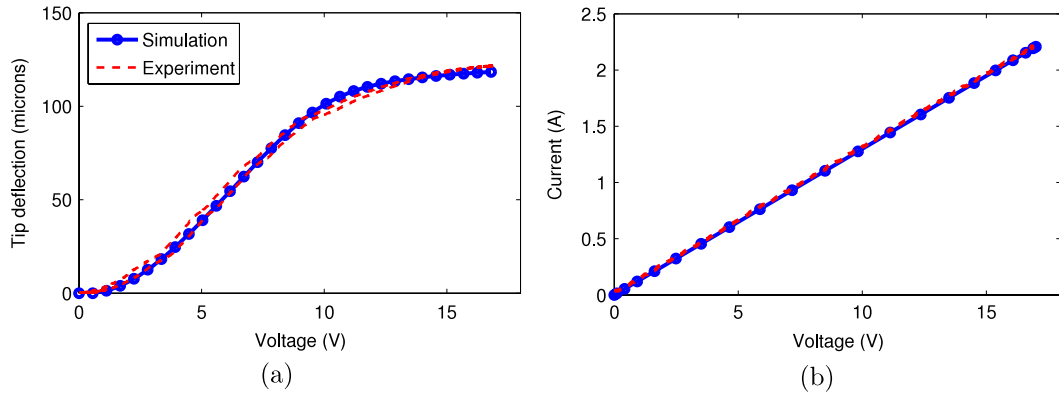


Figure 3. Quasi-static model results: (a) voltage deflection and (b) voltage–current.

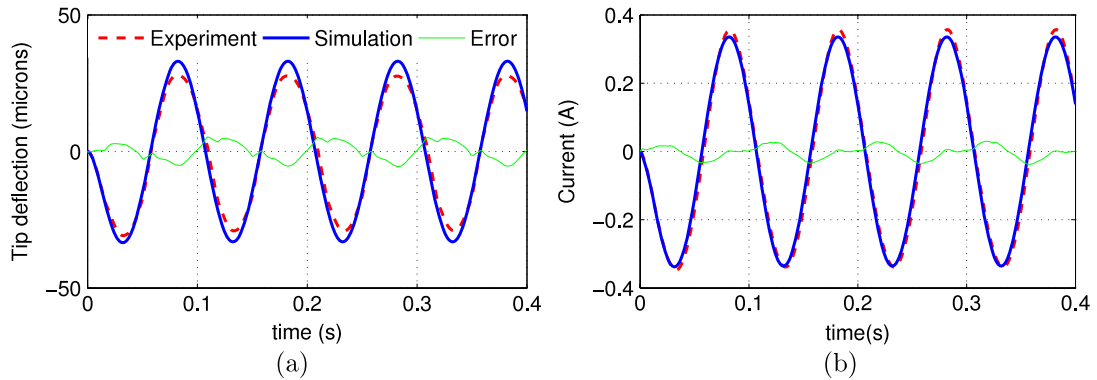


Figure 4. Experimental and model results at 10 Hz: (a) tip displacement and (b) current.

the harmonic excitation is switched on, the fundamental mode is also excited which interacts with components at the drive frequency, giving rise to beats. The current takes a few cycles to reach steady state and the response looks typical of a damped second-order system.

6. Nonlinear dynamic solution procedure

Solution of nonlinear dynamic systems is a particularly challenging task as even unconditionally stable time-integration approaches for linear systems may become unstable. The governing equations for the finite element system described in section 2 can be written as

$$\mathbf{M}\ddot{\mathbf{U}} + \mathbf{D}\dot{\mathbf{U}} = \mathbf{R}(t) - \mathbf{F}(\mathbf{U}, t), \quad (43)$$

where the mass matrix \mathbf{M} , damping matrix \mathbf{D} , and state vector \mathbf{U} are of the form

$$\mathbf{M} = \begin{bmatrix} \mathbf{0} & \mathbf{0} \\ \mathbf{0} & \mathbf{M}^u \end{bmatrix}, \quad \mathbf{D} = \begin{bmatrix} \mathbf{D}^A & \mathbf{0} \\ \mathbf{0} & \mathbf{D}^u \end{bmatrix}, \quad (44)$$

$$\mathbf{U} = \begin{pmatrix} \mathbf{Q}^A \\ \mathbf{Q}^u \end{pmatrix}.$$

The vector of externally applied forces $\mathbf{R}(t)$ includes contributions from the coil source current density and/or traction on certain boundaries; $\mathbf{F}(\mathbf{U}, t)$ is the internal nodal force vector whose derivative with respect to the state vector \mathbf{U} yields the stiffness matrix. Since \mathbf{F} contains contributions from magnetic field and stress which are nonlinearly dependent on \mathbf{U} , the stiffness matrix \mathbf{K} is also state-dependent. Evaluation of

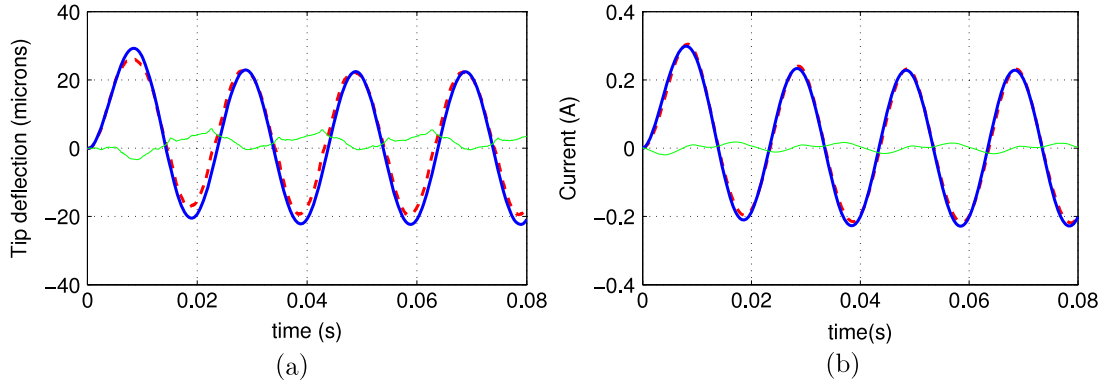


Figure 5. Experimental and model results at 50 Hz: (a) tip displacement and (b) current.

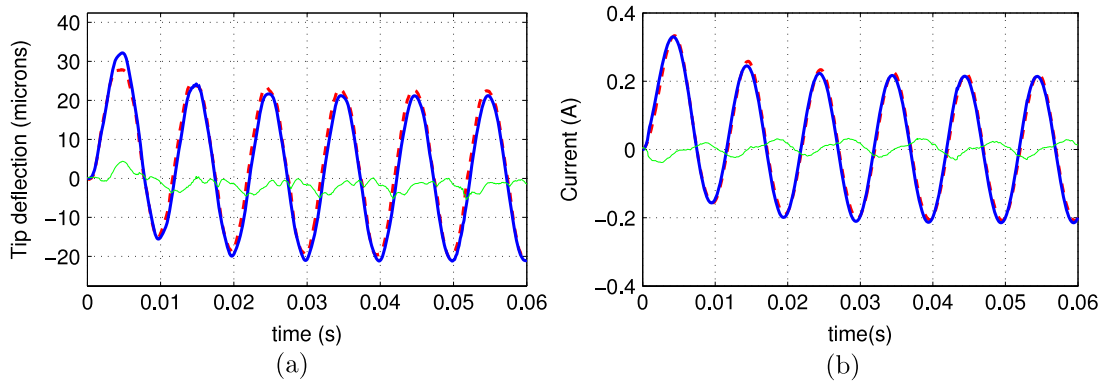


Figure 6. Experimental and model results at 100 Hz: (a) tip displacement and (b) current.

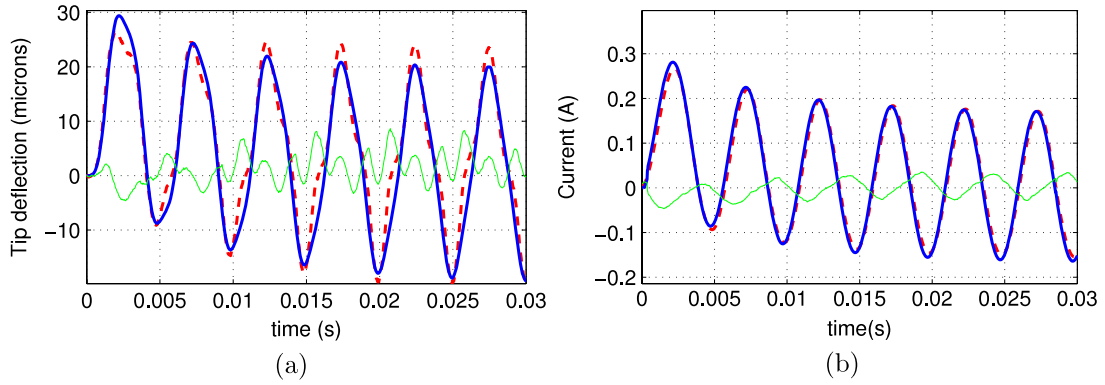


Figure 7. Experimental and model results at 200 Hz: (a) tip displacement and (b) current.

\mathbf{F} and \mathbf{K} is the most time-consuming operation in the solution process.

Bathe [18] suggested various time-integration approaches for nonlinear structural problems of a similar form. Explicit methods are ruled out since the mass matrix is singular. An implicit scheme based on the trapezoidal rule is implemented, combined with equilibrium iterations. At the k th iteration the system equations can be written as

$$\mathbf{M}^{t+\Delta t} \ddot{\mathbf{U}}^{(k)} + \mathbf{D}^{t+\Delta t} \dot{\mathbf{U}}^{(k)} + {}^{t+\Delta t} \mathbf{K}^{(k-1)} \Delta \mathbf{U}^{(k)} = {}^{t+\Delta t} \mathbf{R} - {}^{t+\Delta t} \mathbf{F}^{(k-1)}, \quad (45)$$

$${}^{t+\Delta t} \mathbf{U}^{(k)} = {}^{t+\Delta t} \mathbf{U}^{(k-1)} + \Delta \mathbf{U}^{(k)}. \quad (46)$$

According to the trapezoidal rule of time integration, the

following assumptions are used:

$${}^{t+\Delta t} \mathbf{U} = {}^t \mathbf{U} + \frac{\Delta t}{2} ({}^t \dot{\mathbf{U}} + {}^{t+\Delta t} \dot{\mathbf{U}}), \quad (47)$$

$${}^{t+\Delta t} \dot{\mathbf{U}} = {}^t \dot{\mathbf{U}} + \frac{\Delta t}{2} ({}^t \ddot{\mathbf{U}} + {}^{t+\Delta t} \ddot{\mathbf{U}}). \quad (48)$$

The vectors $\ddot{\mathbf{U}}^{(k)}$ and $\dot{\mathbf{U}}^{(k)}$ can be written using (46)–(48) as

$${}^{t+\Delta t} \ddot{\mathbf{U}}^{(k)} = \frac{4}{\Delta t^2} ({}^{t+\Delta t} \mathbf{U}^{(k-1)} - {}^t \mathbf{U} + \Delta \mathbf{U}^{(k)}) - \frac{4}{\Delta t} {}^t \dot{\mathbf{U}} - {}^t \ddot{\mathbf{U}}, \quad (49)$$

$${}^{t+\Delta t} \dot{\mathbf{U}}^{(k)} = \frac{2}{\Delta t} ({}^{t+\Delta t} \mathbf{U}^{(k-1)} - {}^t \mathbf{U} + \Delta \mathbf{U}^{(k)}) - {}^t \dot{\mathbf{U}}. \quad (50)$$

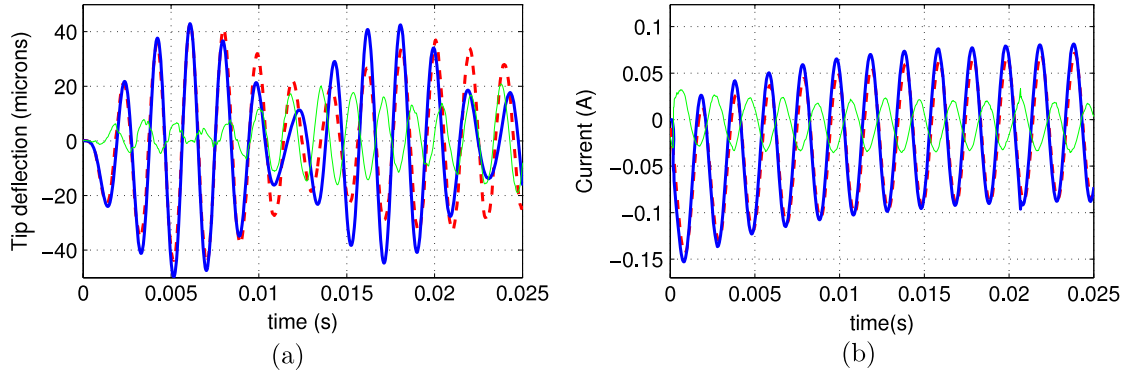


Figure 8. Experimental and model results at 500 Hz: (a) tip displacement and (b) current.

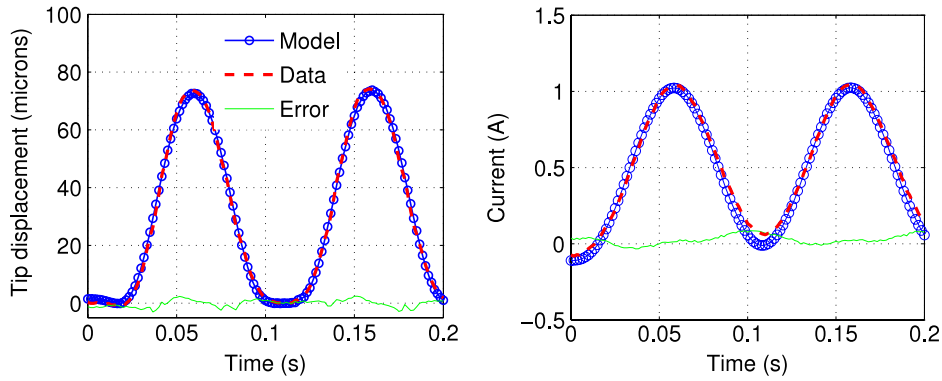


Figure 9. Actuator response to harmonic excitation at 10 Hz.

Substitution in (45) yields the equation of motion for the system,

$$\begin{aligned} & \left[{}^{t+\Delta t}\mathbf{K}^{(k-1)} + \frac{4\mathbf{M}}{\Delta t^2} + \frac{2\mathbf{D}}{\Delta t} \right] \Delta \mathbf{U}^{(k)} \\ &= {}^{t+\Delta t}\mathbf{R} - \mathbf{M} \left[\frac{4}{\Delta t^2} ({}^{t+\Delta t}\mathbf{U}^{(k-1)} - {}^t\mathbf{U}) - \frac{4}{\Delta t} {}^t\dot{\mathbf{U}} - {}^t\ddot{\mathbf{U}} \right] \\ & - \mathbf{D} \left[\frac{2}{\Delta t} ({}^{t+\Delta t}\mathbf{U}^{(k-1)} - {}^t\mathbf{U}) - {}^t\dot{\mathbf{U}} \right] - {}^{t+\Delta t}\mathbf{F}^{(k-1)}. \end{aligned} \quad (51)$$

The starting values for the internal force and state vector are considered to be the same as the corresponding final values of the previous time step:

$${}^{t+\Delta t}\mathbf{F}^{(0)} = {}^t\mathbf{F}, \quad {}^{t+\Delta t}\mathbf{U}^{(0)} = {}^t\mathbf{U}. \quad (52)$$

The convergence criteria used in this work are based on energy and norm of the out-of-balance load vector [18]. Mathematically, these criteria can be written as

$$\begin{aligned} & \frac{\| {}^{t+\Delta t}\mathbf{R} - {}^{t+\Delta t}\mathbf{F}^{(k-1)} - \mathbf{M} {}^{t+\Delta t}\ddot{\mathbf{U}}^{(k-1)} - \mathbf{D} {}^{t+\Delta t}\dot{\mathbf{U}}^{(k-1)} \|}{\text{RNORM}} \\ & \leq \text{RTOL}, \\ & \frac{\Delta \mathbf{U}^{(k)} \cdot ({}^{t+\Delta t}\mathbf{R} - {}^{t+\Delta t}\mathbf{F}^{(k-1)} - \mathbf{M} {}^{t+\Delta t}\ddot{\mathbf{U}}^{(k-1)} - \mathbf{D} {}^{t+\Delta t}\dot{\mathbf{U}}^{(k-1)})}{\Delta \mathbf{U}^{(1)} \cdot ({}^{t+\Delta t}\mathbf{R} - {}^t\mathbf{F} - \mathbf{M} {}^t\ddot{\mathbf{U}} - \mathbf{D} {}^t\dot{\mathbf{U}})} \\ & \leq \text{ETOL}. \end{aligned} \quad (53)$$

The mass and damping matrix are state-independent and hence are assembled only once for the entire simulation. The internal

nodal force vector \mathbf{F} and the tangential stiffness matrix \mathbf{K} are assembled in every iteration as they are state-dependent. Evaluation of \mathbf{F} requires computation of the total stress and field for a given flux density and strain distribution, for which the DEAM needs to be inverted. This is done using the quasi-Newton SR1 formula which updates the Jacobian inverse directly, eliminating the need for matrix inversion within the iteration loop. The computed Jacobian inverse in the final iteration of the inversion process is used for the assembly of the global stiffness matrix. Thus, the material model is inverted only once for every integration point and the values of the 3 field components, 6 stress components and 81 terms of the material Jacobian inverse matrix are stored in a global data structure in Matlab. Since COMSOL cannot take vector-valued inputs from Matlab functions, it calls the same function multiple times to assemble the matrices. The material model is coded up such that it is executed only once for a particular set of input values and returns directly from the stored data structure for the remaining number of times.

7. Nonlinear dynamic model results

The same Galfenol unimorph actuator (figure 2) is used to validate the nonlinear dynamic solution procedure. Harmonic excitations ranging from 10 to 200 Hz are applied to the system in the form $V(t) = -V_{\text{bias}} + V_0(1 - \cos(2\pi ft))$. The finite element model is run only for the time duration of the

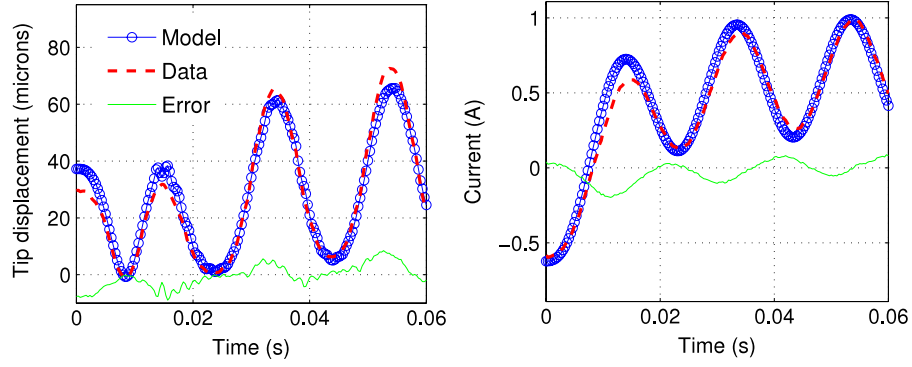


Figure 10. Actuator response to harmonic excitation at 50 Hz.

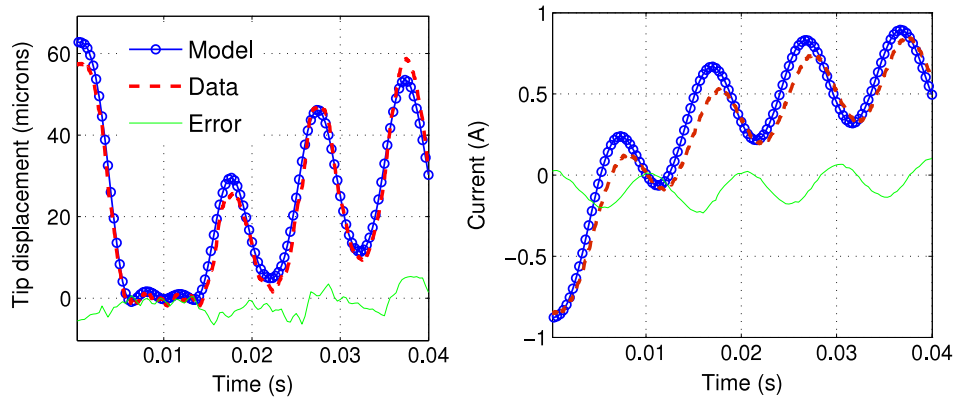


Figure 11. Actuator response to harmonic excitation at 100 Hz.

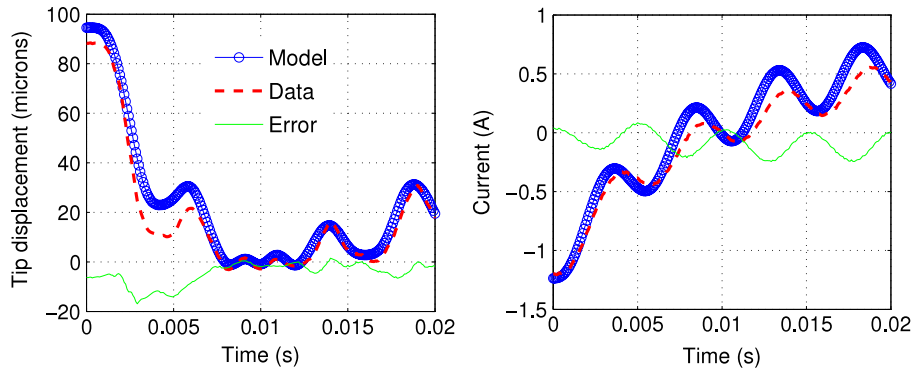


Figure 12. Actuator response to harmonic excitation at 200 Hz.

first few cycles. In order to obtain appreciable displacement response from the beam at higher frequencies, a negative bias voltage (V_{bias}) is applied first before applying the harmonic signal. This ensures that the effective bias point of the cyclic signal is in the burst region. In the model the bias point is obtained in similar fashion by applying the bias voltage smoothed using a hyperbolic tangent function for ease of convergence. Figures 9–12 show the transient response of the transducer for harmonic inputs at 10, 50, 100 and 200 Hz. The modeled responses show good correlation with the experiments, particularly for the tip deflection response. An interesting outcome of nonlinear Galfenol behavior can be seen

where the quadratic nonlinearity of the magnetostrictive strain at zero field causes frequency doubling in the tip deflection response.

8. Concluding remarks

This paper presents a finite element framework for modeling 3D Galfenol transducers driven over nonlinear regimes with dynamic inputs. Weak form equations derived from Maxwell's equations for electromagnetic systems and Navier's equation for mechanical systems are coded into COMSOL, which is used for meshing, global assembly of matrices, and

post-processing. Galfenol constitutive behavior is incorporated using a nonlinear discrete energy-averaged model. A piecewise linear solution procedure is developed in which the solution is obtained in the form of piecewise increments. Galfenol is modeled using linear piezomagnetic equations within each incremental step. The coefficients are updated at the end of each step by analytical differentiation of the constitutive law. Reduction in computational effort is achieved by declaring the material coefficients as interpolated data functions and computing them only at selected locations. The piecewise linear procedure is useful for obtaining a quasi-static system response and accurate bias point determination. A linear dynamic simulation with the Galfenol material coefficients computed at the bias point provides an accurate description of system dynamics for moderate inputs. An implicit time-integration algorithm based on the trapezoidal rule yields the dynamic system response for large-scale inputs. As is required for any vector magnetic-potential-based formulation, the constitutive law is inverted numerically using quasi-Newton iterations. Efficiency is maintained by coding up the material model so that executing the inversion routine once calculates the 6 components of stress, 3 components of field and 81 components of the Jacobian inverse. The inability of COMSOL to accept vector-valued inputs from Matlab functions is overcome by using a global data structure. The model is validated using a Galfenol unimorph actuator. Results show that the modeled responses compare well with experiments and describe the key effects which occur due to the nonlinear behavior of Galfenol.

Acknowledgments

Support for this research is provided by the Office of Naval Research Multidisciplinary University Research Initiative grant # N000140610530. We wish to acknowledge financial support by the member organizations of the Smart Vehicle

Concepts Center (www.SmartVehicleCenter.org), a National Science Foundation Industry/University Cooperative Research Center, and the Smart Vehicle Concepts Center Fellowship Program.

References

- [1] Dapino M, Smith R and Flatau A 2000 *IEEE Trans. Magn.* **36** 545–56
- [2] Huang W, Wang B, Cao S, Sun Y, Weng L and Chen H 2007 *IEEE Trans. Magn.* **43** 1381–4
- [3] Jiles D C 1994 Modeling the effects of eddy current losses on frequency dependent hysteresis loops in electrically conducting media *IEEE Trans. Magn.* **30** 4326–8
- [4] Sarawate N and Dapino M 2008 *Smart Mater. Struct.* **17** 065013
- [5] Benbouzid M, Beguenane R, Reyne G and Meunier G 1997 Finite element modeling of Terfenol-D magneto-mechanical coupling: application to a direct micro-stepping rotary motor *IEEE Electric Machines and Drives Conf.* pp WC2–6
- [6] Kannan K and Dasgupta A 1997 *Smart Mater. Struct.* **6** 341–50
- [7] Zhou H and Zhou Y 2007 *Smart Mater. Struct.* **16** 198–206
- [8] Kim J and Jung E 2005 *Smart Mater. Struct.* **14** 1273–80
- [9] Pérez-Aparicio J and Sosa H 2004 *Smart Mater. Struct.* **13** 493–502
- [10] Slaughter J 2009 Coupled structural and magnetic models: linear magnetostriction in COMSOL *Proc. COMSOL Conf.*
- [11] Mudivartha C, Datta S, Atulasimha J and Flatau A B 2008 *Smart Mater. Struct.* **17** 035005
- [12] Graham F, Mudivartha C, Datta S and Flatau A 2009 *Smart Mater. Struct.* **18** 104013
- [13] Evans P and Dapino M 2011 *IEEE Trans. Magn.* **47** 221–30
- [14] Evans P G and Dapino M J 2010 *J. Appl. Phys.* **107** 063906
- [15] Benbouzid M, Reyne G, Meunier G, Kvarnsjö L and Engdahl G 1995 *IEEE Trans. Magn.* **31** 1821–4
- [16] Armstrong W D 1997 *J. Appl. Phys.* **81** 2321–6
- [17] Atulasimha J, Akhras G and Flatau A 2008 *J. Appl. Phys.* **103** 07–336
- [18] Bathe K 1999 *Finite Element Procedures* (Upper Saddle River, NJ: Prentice-Hall)